Supporting Information for:

The Making and Breaking of Exciton Cooling Bottlenecks in Halide Perovskite Nanocrystals

Jia Wei Melvin Lim[1, †], Yuanyuan Guo[1, †], Minjun Feng[1], Rui Cai[1], Tze Chien Sum[1*]

[1]Division of Physics and Applied Physics, School of Physical and Mathematical Sciences, Nanyang Technological University, 21 Nanyang Link, Singapore 637371, Singapore.

[†]Authors contributed equally

*Email: Tzechien@ntu.edu.sg

Content list:

Supplementary Figures

Figure S1. Size analysis of $CsPbBr_3$ nanocrystals

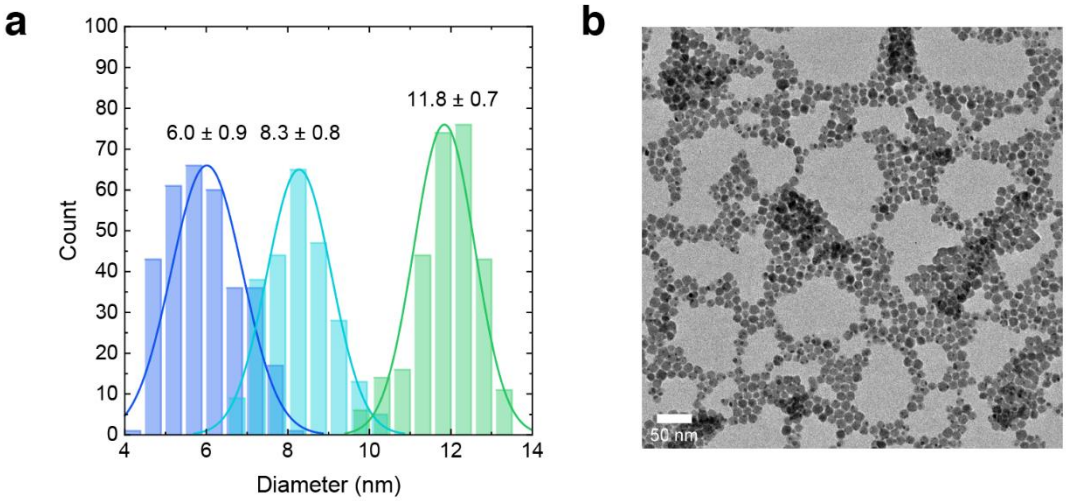

Figure S1: Transmission electron microscopy (TEM) size analysis for $CsPbBr_3$ nanocrystals used in this work. **(a)** The size distribution for all three different sized samples and **(b)** representative TEM image of the nanocrystals. Scale bar: 50 nm.

Figure S2. Size analysis of $MAPbBr_3$ and $FAPbBr_3$ nanocrystals

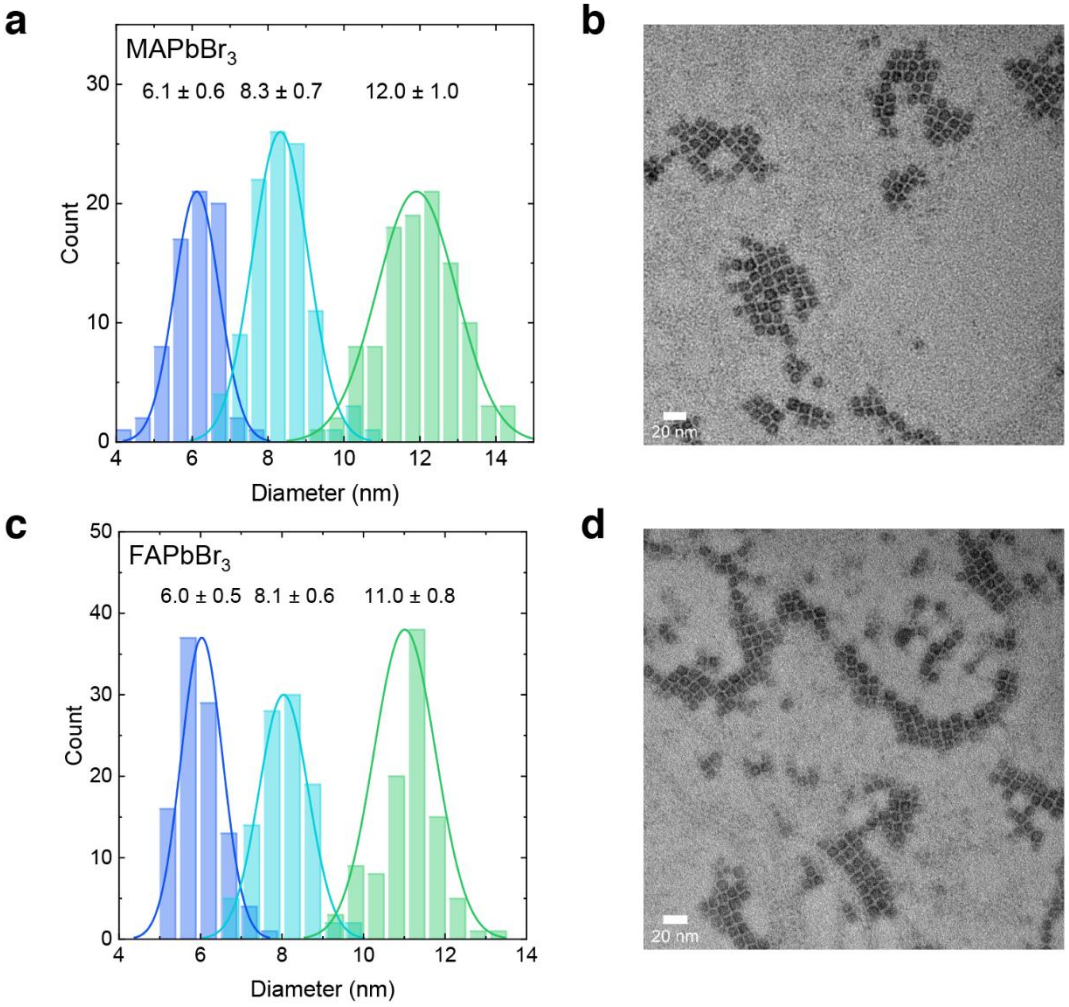

Figure S2: Transmission electron microscopy (TEM) size analysis for $MAPbBr_3$ and $FAPbBr_3$ nanocrystals used in this work. **(a) and (c)** The size distribution for all three different sized samples and **(b) and (d)** representative TEM image of the nanocrystals for $MAPbBr_3$ and $FAPbBr_3$ respectively. Scale bar: 20 nm.

Figure S3. Linear absorption spectra of MA- and $FAPbBr_3$ nanocrystals

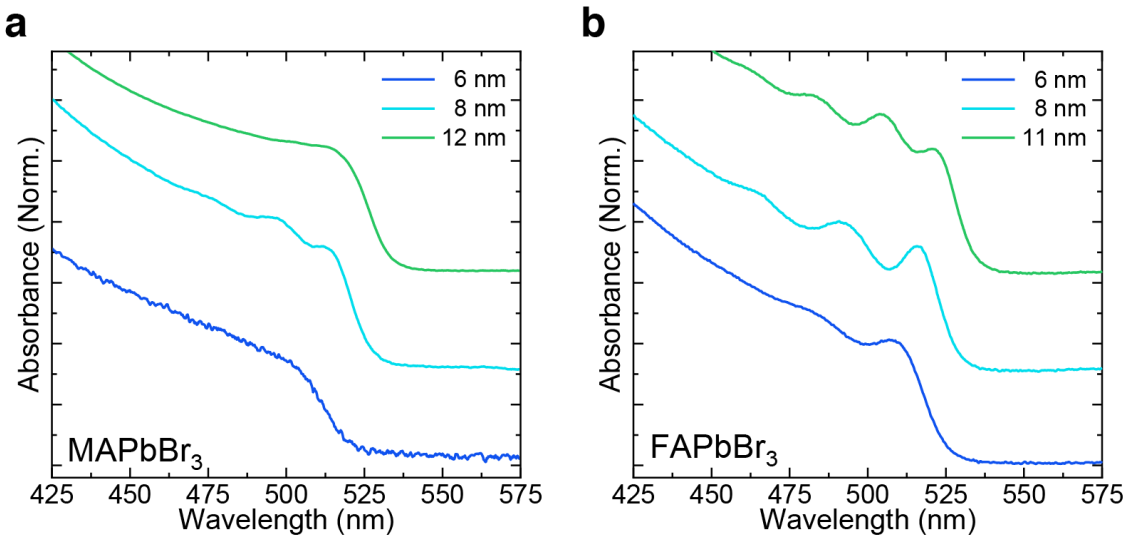

Figure S3: Linear absorption spectra for **(a)** $MAPbBr_3$ and **(b)** $FAPbBr_3$ nanocrystals used in this work.

Figure S4. Pump-probe plots of 6 and 12 nm $CsPbBr_3$ nanocrystals.

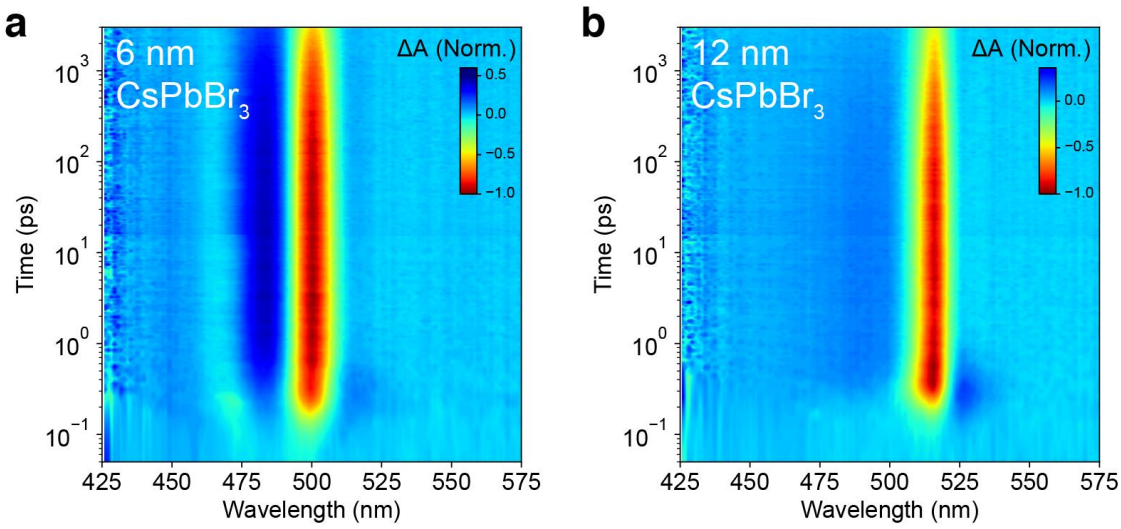

Figure S4: Representative pseudocolour pump-probe plots of **(a)** 6 nm and **(b)** 12 nm $CsPbBr_3$ nanocrystals collected with 470 nm pump excitation at a low fluence corresponding to $\langle N \rangle \sim 0.10$.

Figure S5. Fluence dependent rise time dynamics of $CsPbBr_3$ nanocrystals

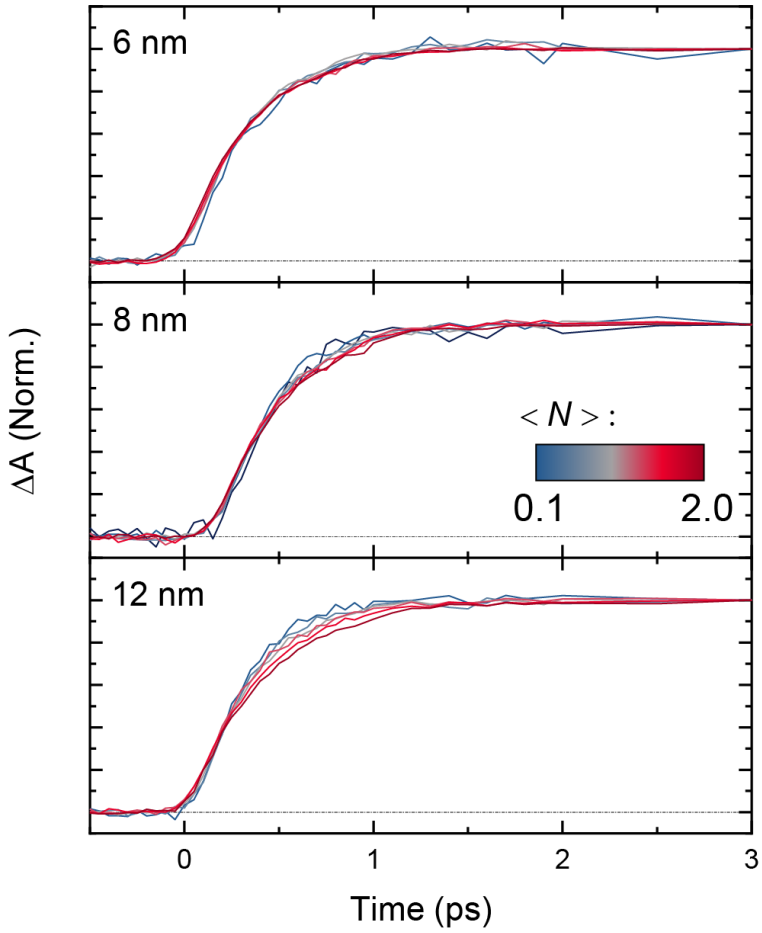

Figure S5: Rise time dynamics of the main photobleaching peak in the pump-probe spectra of the three sizes of $CsPbBr_3$. The spectra were collected with 400 nm excitation in a range of fluences corresponding to $\langle N \rangle \sim 0.1 - 2.0$.

Figure S6. Size-dependent rise time dynamics of MA-/FA-$PbBr_3$ nanocrystals

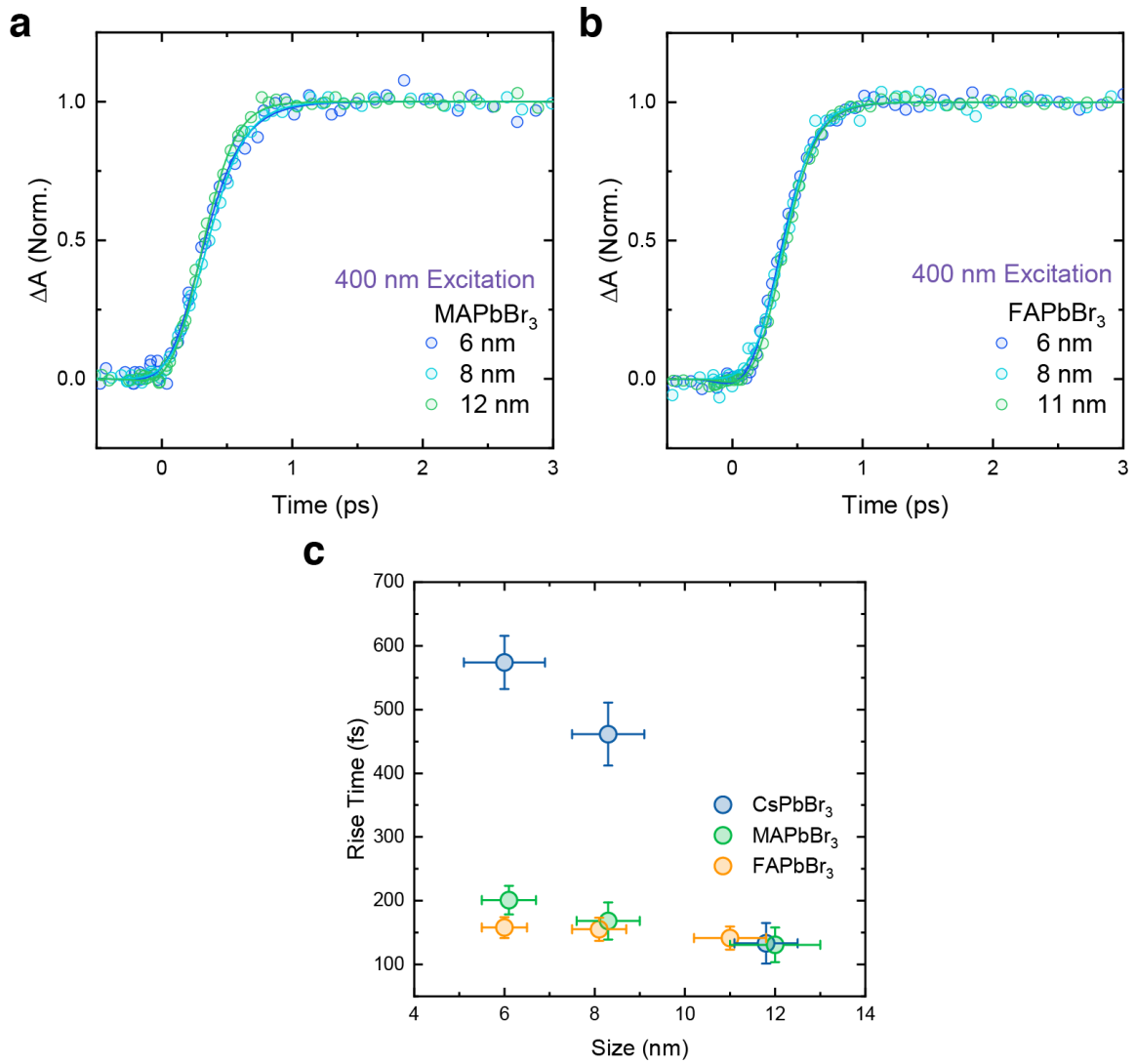

Figure S6: Rise time dynamics of the main photobleaching peak in the pump-probe spectra of three sizes of **(a)** $MAPbBr_3$ and **(b)** $FAPbBr_3$. The spectra were collected with 400 nm excitation at low fluence corresponding to $\langle N \rangle \ll 1.0$ **(c)** Summary plot of the fitted TA rise times obtained for all nanocrystal compositions and sizes.

Figure S7. Push–probe solvent response kinetics

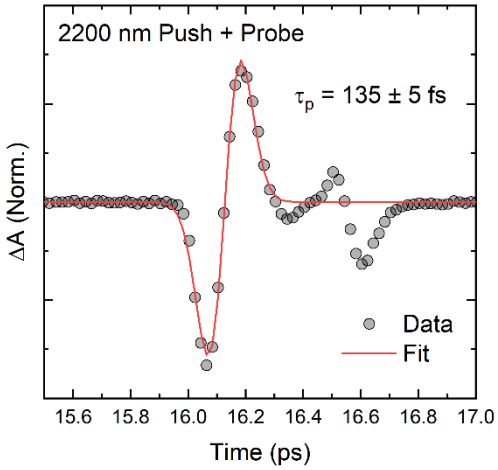

Figure S7: Fitted solvent response obtained using a push wavelength of 2200 nm and monitored at probe wavelength of 512 nm. The extracted push pulse duration is 135 ± 5 fs. Note that the short-lived ringing after 16.4 ps can be observed here because the fluence is ~5.0 mJ/cm^2, far higher than that used in our experiments (< 3.0 mJ/cm^2), where such ringing is not observed.

Figure S8. Pump–probe plots of 8 nm NCs in the presence of the push pulse

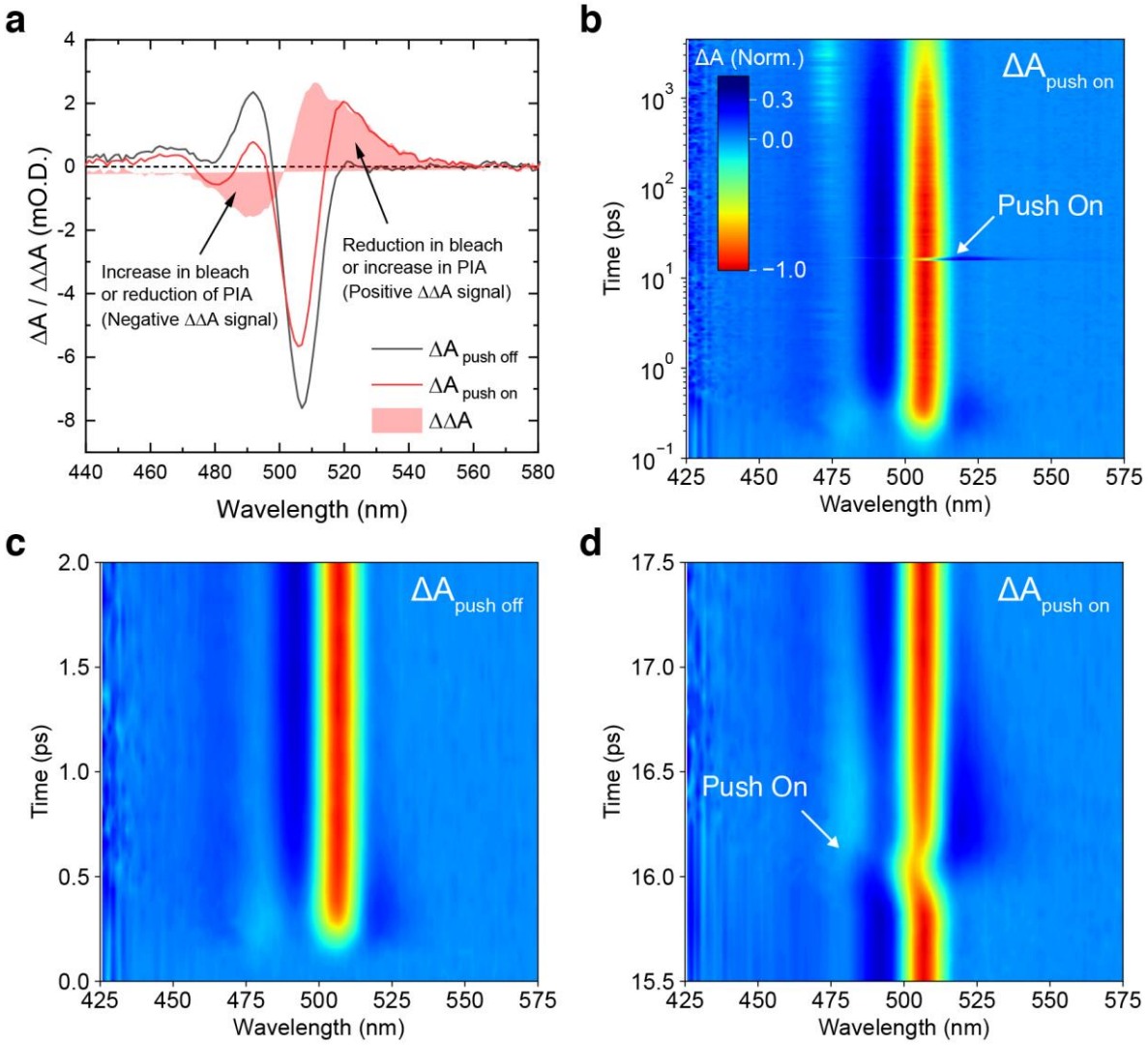

Figure S8 Push-induced effect on the PP spectrum of 8 nm $CsPbBr_3$ NCs. **(a)** The relationship between ΔΔA, $\Delta A_{push\ on}$ and $\Delta A_{push\ off}$. ΔΔA was calculated by taking $\Delta\Delta A = \Delta A_{push\ on} - \Delta A_{push\ off}$. Hence, a positive ΔΔA signal indicates a reduction of a bleach signal or an increase in PIA signal with the push pulse, while conversely a negative ΔΔA signal indicates an increase in the bleach signal or a reduction in PIA signal in presence of the push. **(b)** PPP spectra of $CsPbBr_3$ NCs in a 4.5 ns time window with the presence of the 2200 nm push pulse. The arrow indicates the onset of push arrival. **(c)** Spectra in **(b)** zoomed into the first 2 picoseconds illustrating hot carrier cooling effects on the spectral features. **(d)** Spectra in **(b)** zoomed into the time windows of 15.5 – 17.5 ps illustrating the effect of the push pulse. The spectra were collected with pump wavelength of 470 nm at fluence equivalent to $\langle N \rangle \sim 0.1$ and push wavelength of 2200 nm at 5.0 mJ/cm^2. A high push fluence was used to clearly highlight the effect of the push.

Figure S9. Push–probe plots for nanocrystal samples

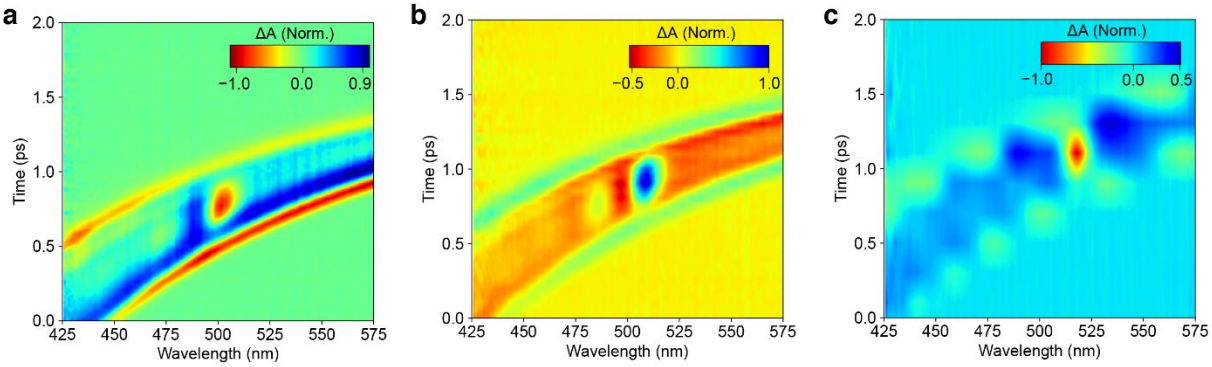

Figure S9: Normalized pseudocolor contour plots of the push–probe spectra obtained for **(a)** 6 nm **(b)** 8 nm and **(c)** 12 nm $CsPbBr_3$ colloidal nanocrystal solutions collected using a push fluence of ~5.0 mJ/cm^2, which is much higher than the range of push fluences used in our experiments. The spectra were collected by placing the chopper in the path of the push beam. No multi-photon absorption induced signals was observed at this high push fluence, while a minor contribution from the optical Stark effect around the region corresponding to the bandgap value of the PNCs within the pulse duration can be observed. This effect can be minimized by limiting the push fluences below some threshold value of ~3.0 mJ/cm^2 and occurs within the pulse duration (~150 fs), and hence will not affect the relaxation dynamics.

Figure S10. Push fluence dependence on the fraction of pushed carriers

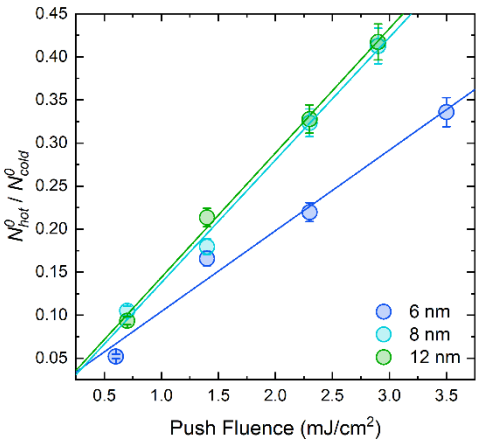

Figure S10: Dependence of the fraction of pushed hot carriers (N^0_{hot}/N^0_{cold}) on the push fluence for all three sizes of $CsPbBr_3$ nanocrystals. The solid lines are linear fits to the data.

Figure S11. Push fluence dependent PPP kinetics

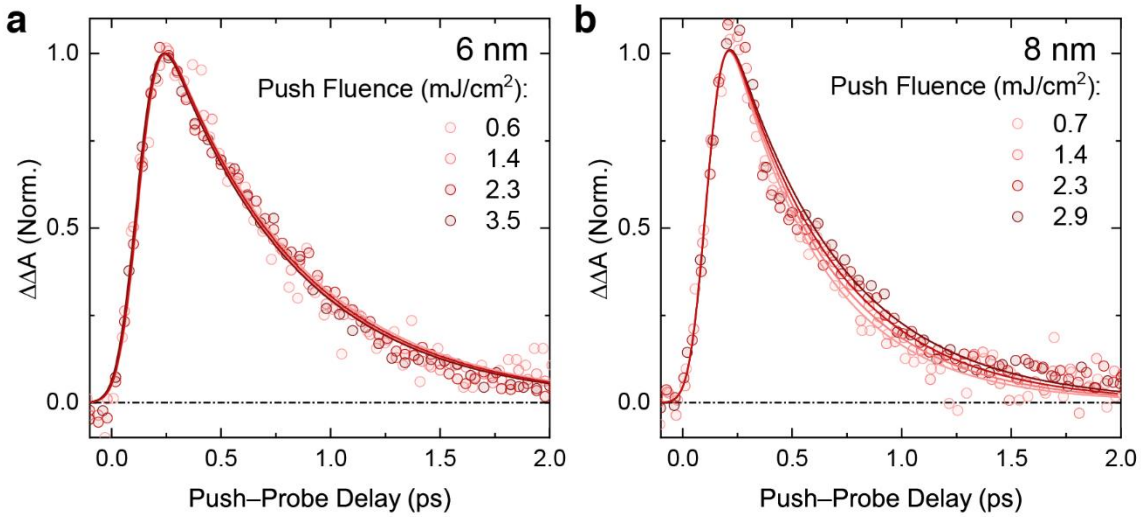

Figure S11: Push fluence dependent PPP delta kinetics at the XB1 peak for **(a)** 6 nm and **(b)** 8 nm $CsPbBr_3$ nanocrystals. The pump fluence was kept at values corresponding to $\langle N \rangle \sim 0.1$.

Figure S12. Difference analyses of push-induced spectral changes

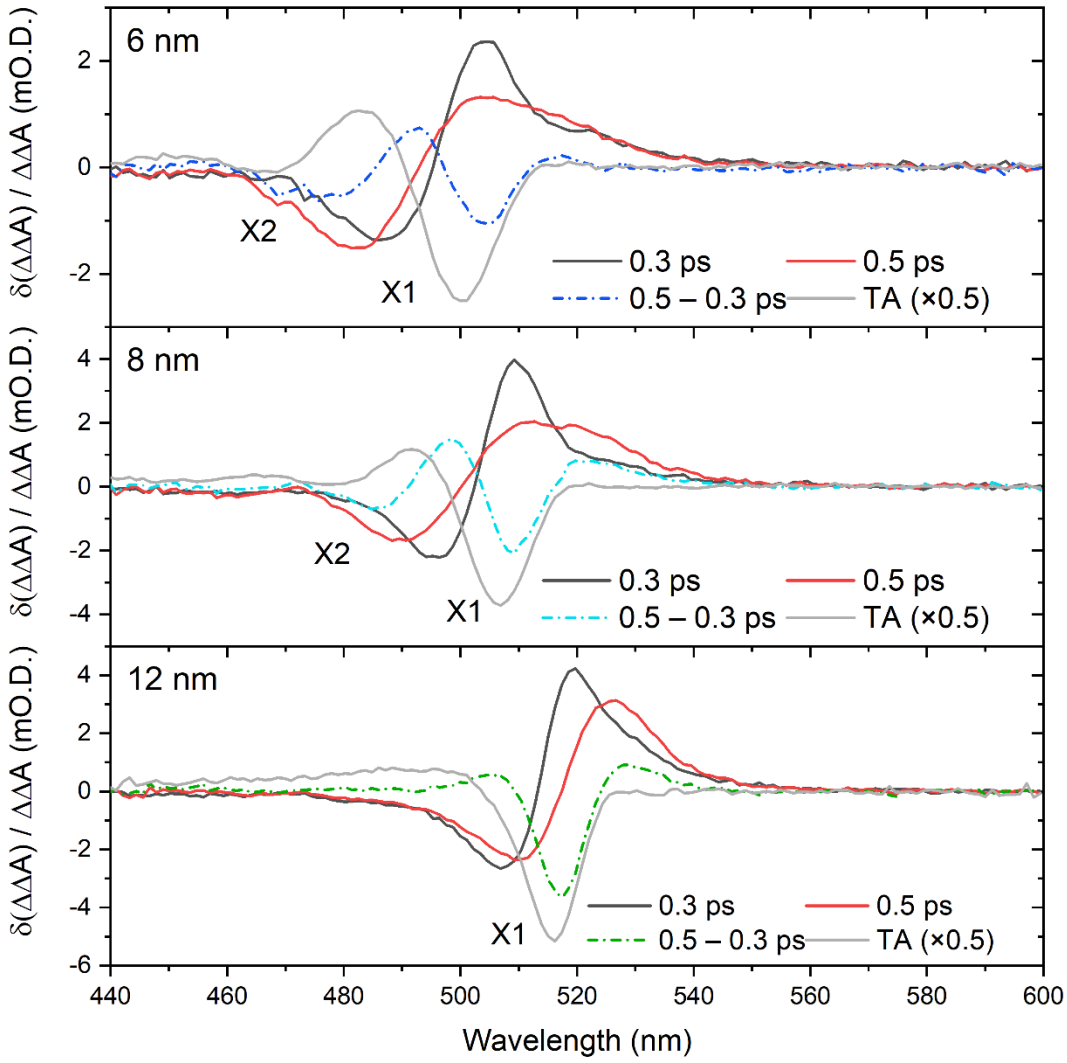

Figure S12: Difference analyses of push-induced spectral changes for 6, 8 and 12 nm nanocrystals. The black and red solid lines represent the ΔΔA spectra at 0.3 and 0.5 ps, respectively. The difference spectra (dashed lines) of the two ΔΔA spectra *i.e.* ΔΔA(t = 0.5 ps) – ΔΔA (t = 0.3 ps) reveals a contribution from both X1 and X2 exciton states, perhaps suggesting their participation in the carrier cooling process. The representative pump-probe (TA) spectra are overlaid in gray solid lines to highlight the peak positions.

Figure S13. Pump fluence dependent PPP kinetics

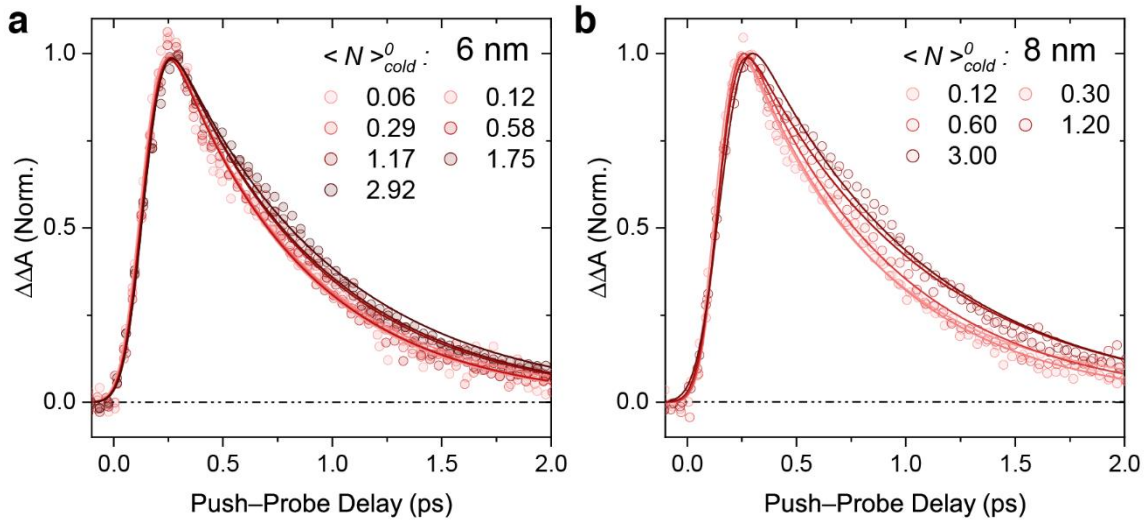

Figure S13: Pump fluence dependent PPP delta kinetics at the XB1 peak for **(a)** 6 nm and **(b)** 8 nm nanocrystals. The pump fluences are expressed as the average number of photogenerated excitons per NC (<*N*>).

Figure S14. Normalized amplitudes of pump fluence dependent changes

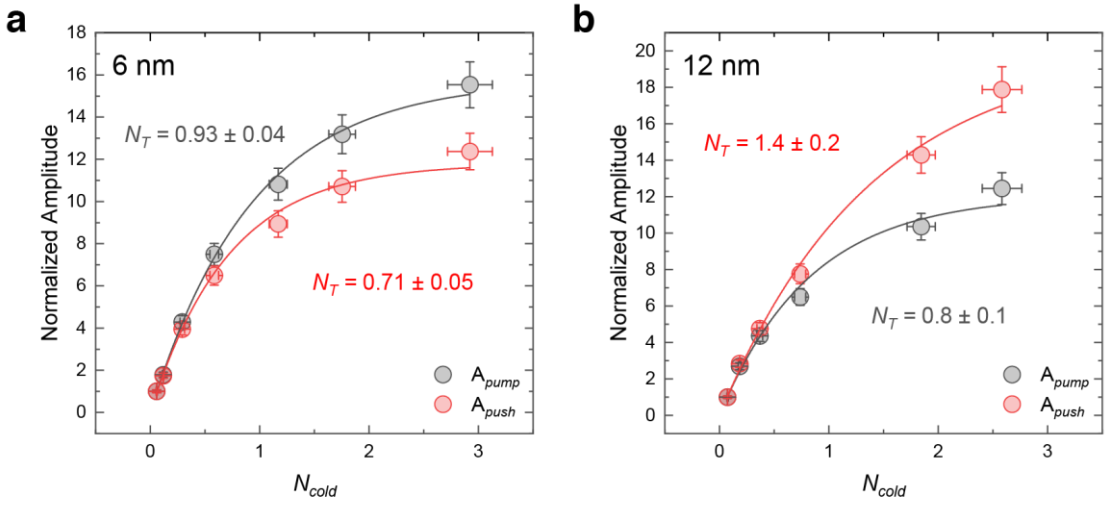

Figure S14: Variation of the pump and push induced bleach amplitudes (A_{pump} and A_{push} respectively) versus N_{cold} (proportional to pump fluence) for **(a)** 6 nm and **(b)** 12 nm nanocrystals. The amplitudes are normalized to their initial value to highlight their saturation behavior. The pump fluences are expressed as the average number of photogenerated excitons per NC (N_{cold}), assuming Poissonian statistics for exciton generation. The amplitudes can be described by a simple phenomenological saturation model, $A \propto 1 - \exp(-N_{cold}/N_T)$, with the saturation threshold density N_T. In 6 nm NCs, A_{pump} increases faster, which leads to an overall decrease in N^0_{hot}/N^0_{cold} with N_{cold}. The reverse trend of A_{push} and A_{pump} is observed for 12 nm NCs, which leads to an increase in N^0_{hot}/N^0_{cold} with N_{cold}, as shown in **Figure 4b** in the main text.

Figure S15. Fluence dependent pump-probe XB1 kinetics

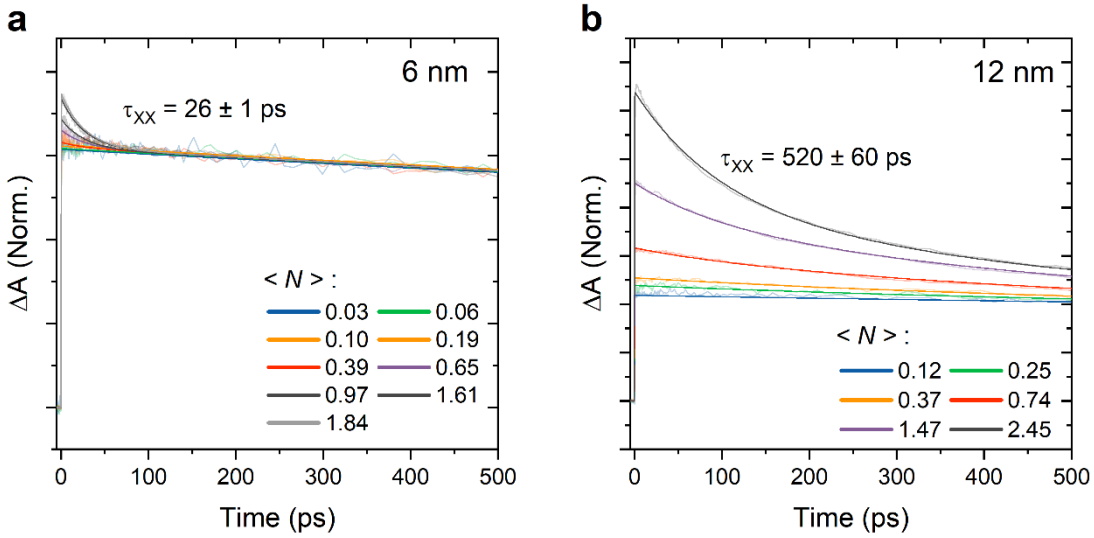

Figure S15: Normalized pump-fluence dependent bleach recovery kinetics for the XB1 peak of **(a)** 6 nm and **(b)** 12 nm $CsPbBr_3$ nanocrystals. The pump-probe spectra were acquired with pump wavelength of 470 nm at several fluences as indicated in the plots. The bold solid lines are global exponential fits to the data to extract the lifetimes. The biexciton Auger recombination lifetime (τ_{XX}) is indicated in the respective plots.

Figure S16. Global fit of fluence dependent pump-probe XB1 kinetics

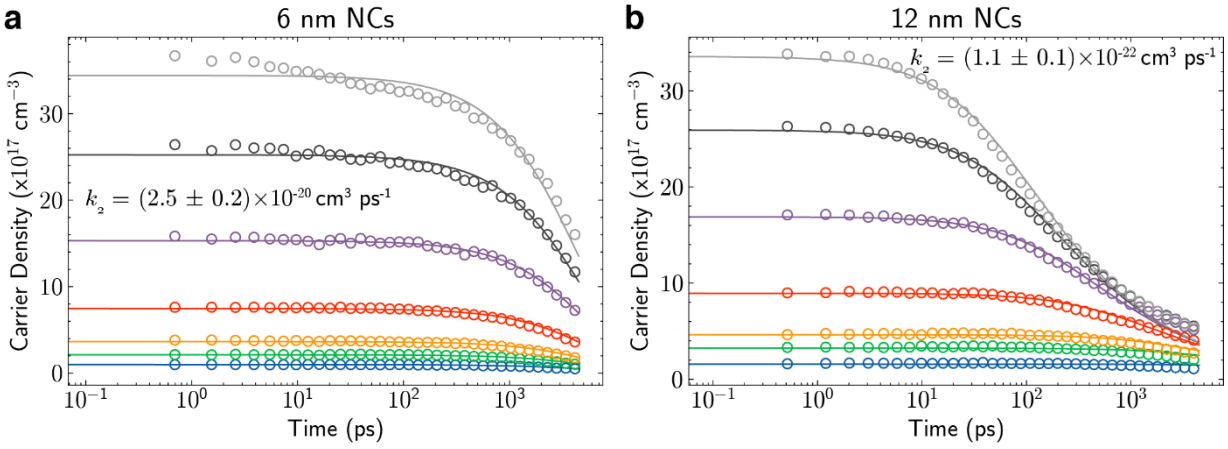

Figure S16: Global fit of the pump-fluence dependent bleach recovery kinetics for the XB1 peak of **(a)** 6 nm and **(b)** 12 nm $CsPbBr_3$ nanocrystals to the kinetic model detailed in **Note 3**. Open circles denote the data points while solid lines denote the fits. The fitted bimolecular recombination rate constants (k_2) are denoted in the respective panels.

Figure S17. Global fit of fluence dependent PPP kinetics

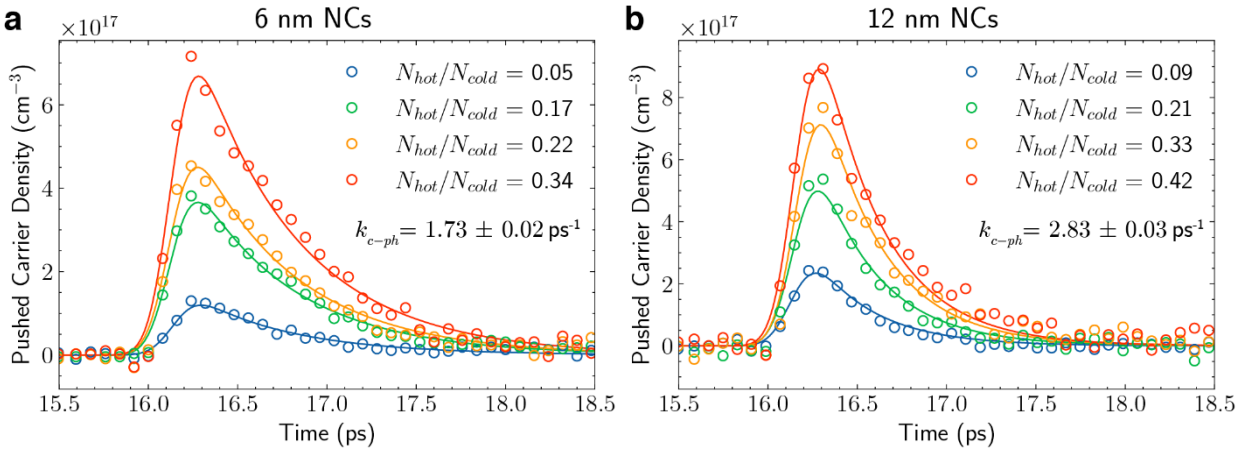

Figure S17: Global fit of the push-fluence dependent push delta for **(a)** 6 nm and **(b)** 12 nm $CsPbBr_3$ nanocrystals to the kinetic model described in the main text (also detailed in **Note 3**). Open circles denote the data points while solid lines denote the fits. The fitted carrier-phonon scattering rate constants (k_{c-ph}) are denoted in the respective panels.

Figure S18. Simulated PPP dynamics from the kinetic model

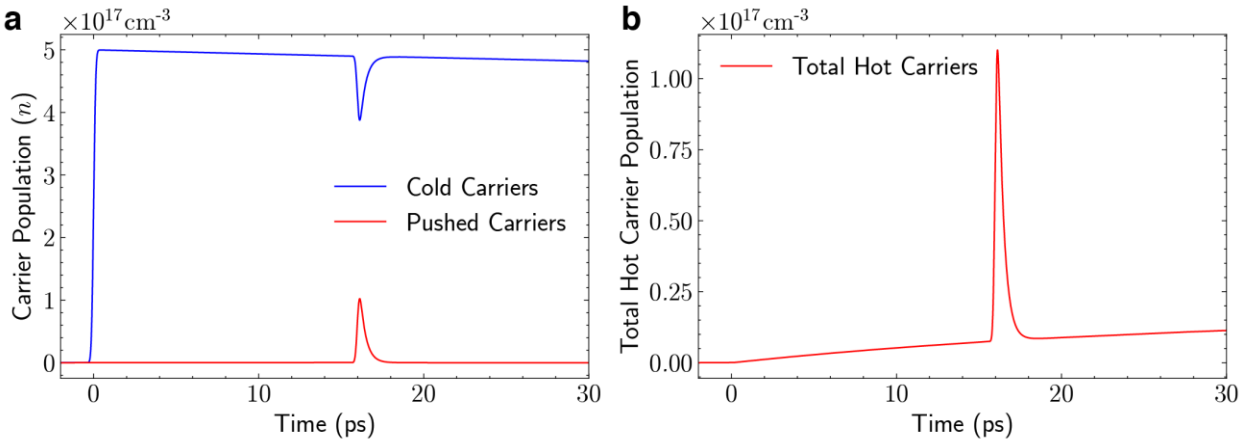

Figure S18: Simulated PPP dynamics obtained with the kinetic model described in **Note 1**. **(a)** Simulated cold and pushed carrier populations over time. **(b)** The total hot carrier density over time.

Supplementary Notes

Note 1. Distinguishing the hot phonon effect and intrinsic phonon bottleneck effect

The *hot phonon* effect and *intrinsic phonon* bottleneck effect are distinct mechanisms that should not be confused with one another. However, they are sometimes simply referred to as the "*phonon bottleneck effect*" in the literature without further elaboration, which causes some confusion. In early reports by the Group III–V and II–VI semiconductor communities, the former mechanism is referred to as the *hot phonon* effect.[1-3] On the other hand, the latter mechanism is referred to as the *phonon bottleneck* effect by the quantum dot community.[4-7] In the halide perovskite community, the *hot phonon* effect is most commonly referred to as "*hot phonon bottleneck*",[8-11] while the latter is referred to as "*intrinsic phonon bottleneck*"[11, 12] or just "*phonon bottleneck*".[13, 14] In this work, we refer to each mechanism as "*hot phonon effect*" and "*intrinsic phonon bottleneck*" respectively to better distinguish them, since we are discussing both effects in this manuscript.

There are several aspects where both effects are distinct, as illustrated in the schematic shown in **Figure S19**. The first is by distinguishing the carrier densities at which each effect starts to dominate. The hot phonon effect, as its name implies, dominates when the material is photoexcited with excess energy and at elevated carrier densities (typically $>10^{18}$ cm^{-3}). Because carrier cooling proceeds in a cascade process of LO phonon emission from hot carriers and the subsequent LO phonon decay, the limiting process becomes the rate-determining step that forms the basis of this "bottleneck". In the case of polar halide perovskites, the efficient LO phonon interactions and small LO phonon energies (< 20 meV in most compositions[15]) cause a fast build-up of nonequilibrium LO phonon population following photoexcitation. Furthermore, the inhibition of the Klemens channel for LO phonon decay increases the net lifetime of the LO phonons.[16] These effects cause a rapid build-up of a *hot phonon* bath that slows down the hot carrier relaxation. However, when the carrier density is low such that the

build-up of a hot phonon population cannot be achieved, the influence of the hot phonon effect will be minimal and the hot carrier relaxation process will only be limited by the intrinsic LO phonon lifetime of the material (hundreds of fs for halide perovskites[11]).

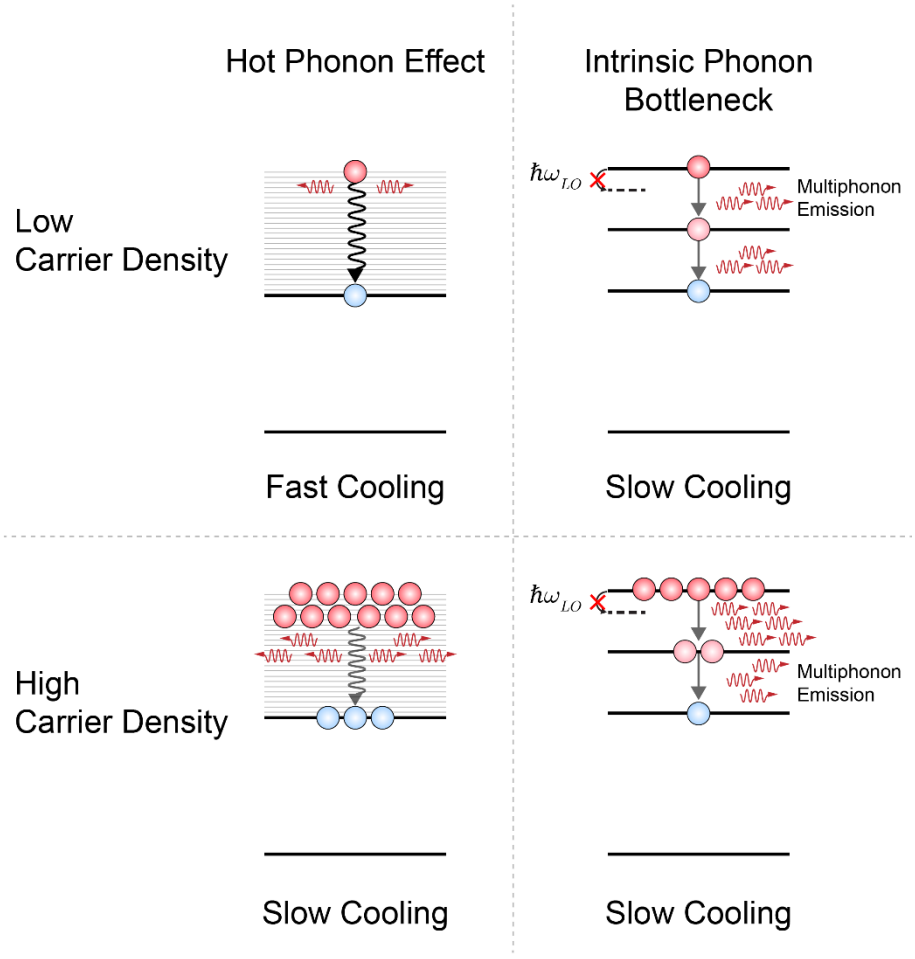

Figure S19: Distinction between the hot phonon and intrinsic phonon bottleneck effect as discussed in the manuscript and in **Note 1**. The physical mechanism that forms the basis of each effect is different and they dominate at different carrier densities.

Meanwhile, the *intrinsic phonon bottleneck* arises because of the discretization of the density of states typically exhibited in semiconductor nanomaterials such as quantum dots, where quantum confinement effects come into play. When a semiconductor shrinks in size, the bulk continuum states start to become more discrete with increased inter-level energy spacing (ΔE).[5, 17] Because of this discretization, hot carrier cooling proceeds *via* these discrete energy steps due to energy conservation. The quantization of phonon energies necessitates hot carrier relaxation to occur through the emission of multiple phonons so that their combined energy is

equal to the energy of the inter-level energy spacing between each successive energy level *i.e.*, $\Delta E = n\hbar\omega$ where n is the number of phonons with frequency ω, as illustrated in **Figure S19**. This multi-phonon emission process is much more inefficient and thus becomes the rate-limiting step in hot carrier relaxation. Therefore, in smaller nanostructures with increasingly strong quantum confinement effects, the inter-energy spacing ΔE increases and so does the number of phonons n required for each successive step which causes the process to become less probable, thereby slowing the hot carrier relaxation. This is the basis behind the mechanism of the *intrinsic phonon* bottleneck. Since this mechanism is only dependent on ΔE and not the phonon build-up, it will dominate the hot carrier relaxation process regardless of the fluence as long as $\Delta E \gg \hbar\omega$. This explains the apparent insensitivity in the cooling dynamics toward the pump fluence dominated by this intrinsic phonon bottleneck as we observed in our study.

Note 2. Detailed discussion regarding the effect of increasing N_{cold}^0

We first start by discussing the case of increasing N_{hot}^0/N_{cold}^0, that is, increasing the push fluence while keeping the pump fluence fixed, as in the case of the push-dependent studies detailed in the main text and **Figure 3**. In this case, the pump fluence is fixed so that the pump-induced cold carrier amplitude A_{pump} is fixed before the push arrival. Then, any changes in the fraction N_{hot}^0/N_{cold}^0 can be straightforwardly ascribed to the change in push fluence and thus N_{hot}^0. In general, N_{hot}^0/N_{cold}^0 increases with push fluence, which is expected because N_{hot}^0 increases with push fluence while N_{cold}^0 is fixed. Therefore, the observed changes in τ_{cool} can be straightforwardly attributed to the action of changing the push fluence. In this work, for example, we observe an increase in τ_{cool}, which we attributed to the increase in pushed hot carriers.

In the case of our pump fluence-dependent experiments, where we vary the pump fluence, and hence, N_{cold}^0, and monitor changes in τ_{cool}, an added complexity arises because changing the pump fluence not only changes A_{pump} but also A_{push} (**Figure S14**). The interpretation would be straightforward as in the case of the push-dependent experiments if A_{push} remains constant while only A_{pump} varies, so any observed trends in τ_{cool} can be directly attributed to the change in N_{cold}^0. In our case, because both A_{pump} and A_{push} varies, we need to consider the dominant factor that drives the change in the fraction of hot-to-cold carriers (N_{hot}^0/N_{cold}^0) or its inverse (N_{cold}^0/N_{hot}^0), which is by examining their saturation behavior. The saturation behavior can be described by a simple phenomenological saturation model, assuming exciton generation in each isolated PNC follows Poissonian statistics. Then, the amplitudes can be described by the equation $A \propto 1 - \exp(-N_{cold}/N_T)$ with N_T being the threshold saturation density.[18] We reiterate our results of the pump-dependent experiments (increasing N_{cold}^0) here for brevity. For all NC sizes, we observe an increase in τ_{cool} with the increase in N_{cold}^0 (**Figure 4a** and

Figure S13). In **Figure 4b** of the main text, for small (6 nm) NCs, we observe that N_{hot}^0/N_{cold}^0 *decreases* with increasing N_{cold}^0. On the other hand, for large (12 nm) NCs, we observe that N_{hot}^0/N_{cold}^0 *increases* with increasing N_{cold}^0. Once again, we reiterate that the observed increase in τ_{cool} cannot be straightforwardly assigned to the increase in N_{cold}^0 here, since N_{hot}^0/N_{cold}^0 changes differently for both sizes. We will discuss the case of each NC size (large and small) separately.

For the small 6 nm NCs, the *decrease* of N_{hot}^0/N_{cold}^0 with N_{cold}^0 can be due to two cases; a dominant increase of N_{cold}^0 or a dominant decrease of N_{hot}^0. We examine the saturation behavior of A_{pump} and A_{push} in **Figure S14a** to verify the likely case here. In **Figure S14a**, we observe that the increase in A_{pump} overshadows the increase in A_{push} because of the larger threshold saturation fluence (N_T) of A_{pump}. This implies that the decrease in $\frac{N_{hot}^0}{N_{cold}^0} = \frac{A_{push}}{A_{pump}}$ is mainly dominated by the more rapid increase in A_{pump}, rather than the latter case. In this case, the observed increase in τ_{cool} should be attributed to the increase in N_{cold}^0.

On the other hand, for the large 12 nm NCs, the *increase* of N_{hot}^0/N_{cold}^0 with N_{cold}^0 can similarly be due to two cases; a dominant increase of N_{hot}^0 or a dominant decrease of N_{cold}^0. Once again, we examine the saturation behavior of A_{pump} and A_{push} in **Figure S14b** to verify the likely case here. In **Figure S14b**, we observe that A_{push} has a larger N_T and hence the increase in A_{push} overshadows the increase in A_{pump}, a trend that is reversed from the small NCs. This implies that the increase in $\frac{N_{hot}^0}{N_{cold}^0} = \frac{A_{push}}{A_{pump}}$ is attributed to the more rapid increase in A_{push} that causes the quantity to diminish with N_{cold}^0. In this case, the observed increase in τ_{cool} should be attributed to the increase in N_{hot}^0.

Therefore, the interpretation of the increase in τ_{cool} with N_{cold}^0 for both NC sizes are different, as discussed in the main text.

Note 3. Details of the kinetic model

The kinetic model described in the main text is based on a system of coupled rate equations each describing a sub-population of the total carrier (exciton) density. Assuming that hot exciton relaxation proceeds *via* the two pathways of exciton–phonon and exciton–exciton scattering interactions, the pushed-induced hot exciton population n_h^{push} can be described by the following differential equation[19]:

$$\frac{dn_h^{push}}{dt} = G^{push}(t) - k_{c-c}\left(n_c - n_h^{total}\right)n_h^{push} - k_{c-ph}n_h^{push} \qquad (1)$$

$G^{push}(t)$ is the generation term describing the effect of the push pulse, k_{c-c} and k_{c-ph} are rate constants for exciton–exciton and exciton–phonon scattering respectively, and total n_c is the cold exciton density. Note that the quantity $n_c - n_h^{total}$ in the second term on the right-hand side represents the total cold excitons at each point in time, which is evaluated by taken the difference between the cold exciton population and *total* HC population n_h^{total}. k_{c-ph} was determined from global fitting of the push-dependent PPP kinetics obtained at low n_c to **Eq. (1)** (**Figure S17**), while the reported value of k_{c-c} (~ 1.1× 10^{-18} cm^3 ps^{-1}) was used.[19] The total hot exciton population is given by n_h^{total} and is the sum of the push-induced HCs and the background HCs from Auger heating (AH) denoted by n_h^{AH}, *i.e.*, $n_h^{total} = n_h^{push} + n_h^{AH}$. We treat n_h^{push} and n_h^{AH} as separate populations because the former, which is induced by the push pulse, describes an initially non-thermalized HC population, while the latter, which results from the energy transfer from the Auger recombination of quasi-thermalized excitons in the pump-induced cold exciton bath, can be treated like a quasi-equilibrium "background" of HCs with a lifetime equal to the Auger heating lifetime. Thus, the population of n_h^{AH} can be described by:

$$\frac{dn_h^{AH}}{dt} = k_2 n_c^2 - k_{cool}^{AH} n_h^{AH} \qquad (2)$$

where $k_{cool}^{AH} \sim \frac{1}{\tau_{AH}}$ is the Auger heating cooling rate constant, and we use a value of τ_{AH} ~ 30 ps for our calculations, according to the values reported in the literature.[12, 16] Generally, the reported value of τ_{AH} is tens of picoseconds, and we found that small changes do not affect the calculations too much so long as the values are in the same order, since $\tau_{AH} \gg \tau_{cool}$. Accordingly, n_h^{total} is described by the following differential equation:

$$\frac{dn_h^{total}}{dt} = \frac{dn_h^{push}}{dt} + \frac{dn_h^{AH}}{dt} \quad (3)$$

It should be noted that in **Eq. (1)**, we assume that the interaction between n_h^{push} and n_h^{AH} is minimal and can be neglected, which is reasonable because n_h^{AH} constitutes only a small fraction of the total exciton population so the dynamics of n_h^{push} is mainly dominated by the interactions with n_c. The cold exciton population n_c is described by the following differential equation, assuming that photogenerated excitons recombine *via* single exciton and exciton–exciton Auger recombination processes:

$$\frac{dn_c}{dt} = G^{pump}(t) - k_1 n_c - k_2 n_c^2 - \frac{dn_h^{push}}{dt} \quad (4)$$

$G^{pump}(t)$ is the generation term describing the effect of the pump pulse, k_1 and k_2 are the monomolecular and bi-molecular rate constants describing the exciton and exciton–exciton Auger recombination, respectively. Here, we have assumed that Auger recombination of excitons scales quadratically,[20] given that the Auger rate in PNCs follows standard volume scaling.[21] k_1 and k_2 were evaluated from the global fitting of the fluence-dependent TA bleach dynamics to **Eq. (4)**, with the exclusion of the push-induced term (**Figure S16**).

The generation term $G(t)$ was modelled as simple Gaussian pulses:

$$G(t) = A \times \exp\left(-\frac{(t-t_0)^2}{2\sigma^2}\right) \quad (5)$$

where t_0 is the arrival or time-zero of the pulse, σ is the pulse width and A is a constant that is proportional to the fluence. Finally, τ_{cool} was evaluated by:[19]

$$\tau_{cool} = \int_{N_h^{push}}^{\frac{N_h^{push}}{e}} \frac{dt}{dn_h^{push}}\, dn_h^{push} \tag{6}$$

where $N_h^{push} = n_h^{push}\left(t = t_0^{push}\right)$ is the initially generated number of hot excitons by the push pulse.

A representative example of the simulated pump-push-probe dynamics is shown in **Figure S18a**, where it can be observed that the simulation reproduces the general shape of the experimental PPP kinetics. From **Figure S18b,** the contribution of HCs from AH to the total HC population is clearly illustrated.

References

(1) Shah, J. Hot electrons and phonons under high intensity photoexcitation of semiconductors. *Solid-State Electronics* **1978**, *21* (1), 43-50. DOI: https://doi.org/10.1016/0038-1101(78)90113-2.

(2) Klimov, V.; Haring Bolivar, P.; Kurz, H. Hot-phonon effects in femtosecond luminescence spectra of electron-hole plasmas in CdS. *Physical Review B* **1995**, *52* (7), 4728-4731. DOI: 10.1103/PhysRevB.52.4728.

(3) Langot, P.; Del Fatti, N.; Christofilos, D.; Tommasi, R.; Vallée, F. Femtosecond investigation of the hot-phonon effect in GaAs at room temperature. *Physical Review B* **1996**, *54* (20), 14487-14493. DOI: 10.1103/PhysRevB.54.14487.

(4) Inoshita, T.; Sakaki, H. Electron-phonon interaction and the so-called phonon bottleneck effect in semiconductor quantum dots. *Physica B: Condensed Matter* **1996**, *227* (1), 373-377. DOI: https://doi.org/10.1016/0921-4526(96)00445-0.

(5) Nozik, A. J. Spectroscopy and hot electron relaxation dynamics in semiconductor quantum wells and quantum dots. *Annual Review of Physical Chemistry* **2001**, *52*, 193-231. DOI: 10.1146/annurev.physchem.52.1.193.

(6) Inoshita, T.; Sakaki, H. Electron relaxation in a quantum dot: Significance of multiphonon processes. *Physical Review B* **1992**, *46* (11), 7260-7263. DOI: 10.1103/PhysRevB.46.7260.

(7) Benisty, H.; Sotomayor-Torrès, C. M.; Weisbuch, C. Intrinsic mechanism for the poor luminescence properties of quantum-box systems. *Physical Review B* **1991**, *44* (19), 10945-10948. DOI: 10.1103/PhysRevB.44.10945.

(8) Yang, Y.; Ostrowski, D. P.; France, R. M.; Zhu, K.; Van De Lagemaat, J.; Luther, J. M.; Beard, M. C. Observation of a hot-phonon bottleneck in lead-iodide perovskites. *Nature Photonics* **2016**, *10* (1), 53.

(9) Yang, J.; Wen, X.; Xia, H.; Sheng, R.; Ma, Q.; Kim, J.; Tapping, P.; Harada, T.; Kee, T. W.; Huang, F. Acoustic-optical phonon up-conversion and hot-phonon bottleneck in lead-halide perovskites. *Nature communications* **2017**, *8*, 14120.

(10) Kahmann, S.; Loi, M. A. Hot carrier solar cells and the potential of perovskites for breaking the Shockley–Queisser limit. *Journal of Materials Chemistry C* **2019**, *7* (9), 2471-2486.

(11) Li, M.; Fu, J.; Xu, Q.; Sum, T. C. Slow Hot-Carrier Cooling in Halide Perovskites: Prospects for Hot-Carrier Solar Cells. *Advanced Materials* **2019**, 1802486.

(12) Li, M.; Bhaumik, S.; Goh, T. W.; Kumar, M. S.; Yantara, N.; Grätzel, M.; Mhaisalkar, S.; Mathews, N.; Sum, T. C. Slow cooling and highly efficient extraction of hot carriers in colloidal perovskite nanocrystals. *Nature communications* **2017**, *8*, 14350.

(13) Li, Y.; Lai, R.; Luo, X.; Liu, X.; Ding, T.; Lu, X.; Wu, K. On the absence of a phonon bottleneck in strongly confined $CsPbBr_3$ perovskite nanocrystals. *Chemical science* **2019**, *10* (23), 5983-5989.

(14) Dai, L.; Deng, Z.; Auras, F.; Goodwin, H.; Zhang, Z.; Walmsley, J. C.; Bristowe, P. D.; Deschler, F.; Greenham, N. C. Slow carrier relaxation in tin-based perovskite nanocrystals. *Nature Photonics* **2021**, *15* (9), 696-702. DOI: 10.1038/s41566-021-00847-2.

(15) Wright, A. D.; Verdi, C.; Milot, R. L.; Eperon, G. E.; Pérez-Osorio, M. A.; Snaith, H. J.; Giustino, F.; Johnston, M. B.; Herz, L. M. Electron–phonon coupling in hybrid lead halide perovskites. *Nature Communications* **2016**, *7* (1), 11755. DOI: 10.1038/ncomms11755.

(16) Fu, J.; Xu, Q.; Han, G.; Wu, B.; Huan, C. H. A.; Leek, M. L.; Sum, T. C. Hot carrier cooling mechanisms in halide perovskites. *Nature communications* **2017**, *8* (1), 1300.

(17) Klimov, V. I. Spectral and dynamical properties of multiexcitons in semiconductor nanocrystals. *Annu Rev Phys Chem* **2007**, *58*, 635-673. DOI: 10.1146/annurev.physchem.58.032806.104537.

(18) Feng, M.; Ye, S.; Lim, J. W. M.; Guo, Y.; Cai, R.; Zhang, Q.; He, H.; Sum, T. C. Insights to Carrier-Phonon Interactions in Lead Halide Perovskites via Multi-Pulse Manipulation. *Small* **2023**, e2301831. DOI: 10.1002/smll.202301831.

(19) Hopper, T. R.; Jeong, A.; Gorodetsky, A. A.; Krieg, F.; Bodnarchuk, M. I.; Huang, X.; Lovrincic, R.; Kovalenko, M. V.; Bakulin, A. A. Kinetic modelling of intraband carrier relaxation in bulk and nanocrystalline lead-halide perovskites. *Physical Chemistry Chemical Physics* **2020**, *22* (31), 17605-17611.

(20) Klimov, V. I. Mechanisms for Photogeneration and Recombination of Multiexcitons in Semiconductor Nanocrystals: Implications for Lasing and Solar Energy Conversion. *The Journal of Physical Chemistry B* **2006**, *110* (34), 16827-16845. DOI: 10.1021/jp0615959.

(21) Li, Y.; Ding, T.; Luo, X.; Chen, Z.; Liu, X.; Lu, X.; Wu, K. Biexciton Auger recombination in mono-dispersed, quantum-confined $CsPbBr_3$ perovskite nanocrystals obeys universal volume-scaling. *Nano Research* **2019**, *12* (3), 619-623. DOI: 10.1007/s12274-018-2266-7.